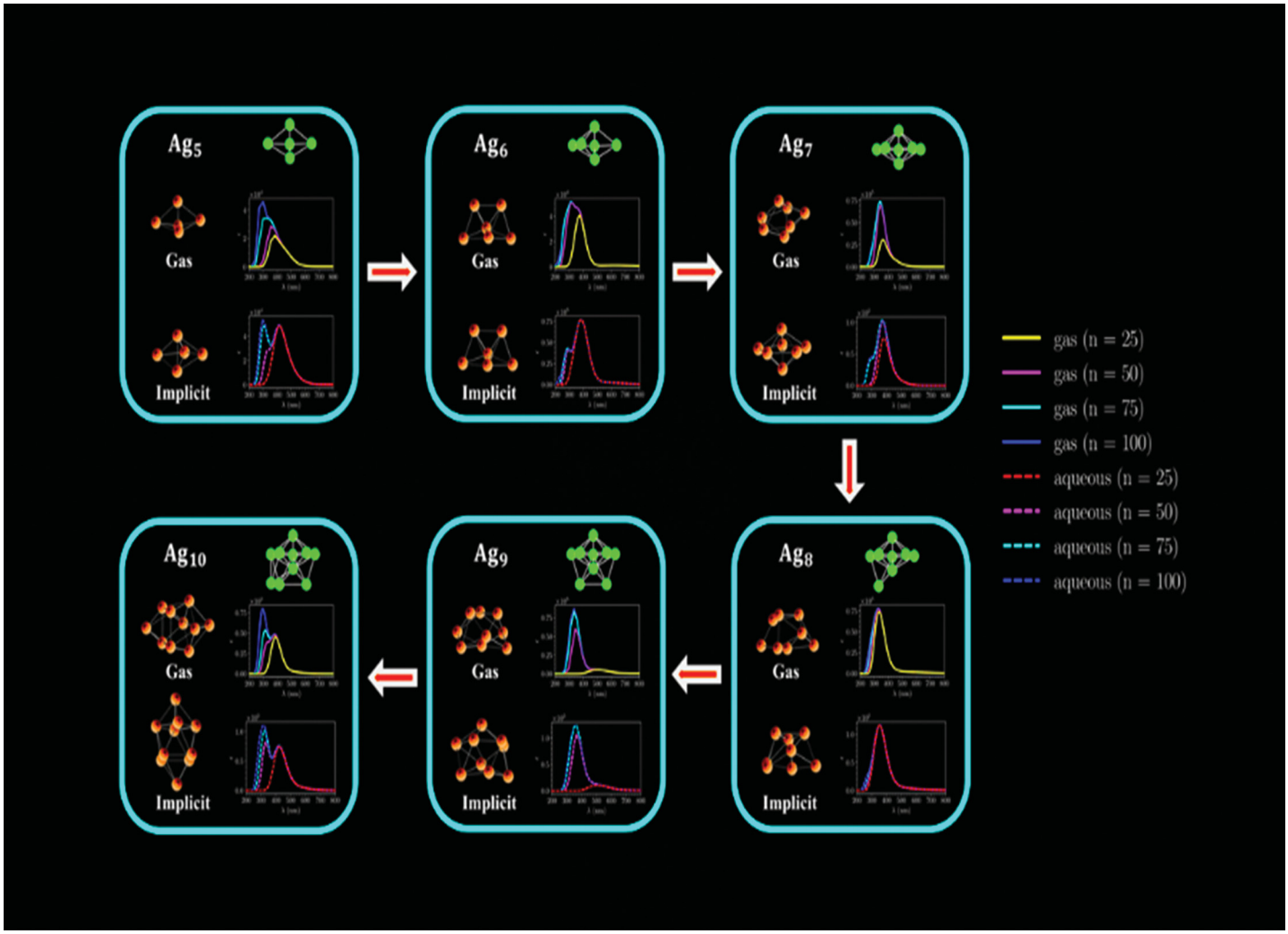

Showcasing research from Professor Jayendran Rasaiah and his group, Mohsen Farshad and Duwage C. Perera at the University of Maine, Orono ME 04469.

Theoretical study of the stability, structure, and optical spectra of small silver clusters and their formation using density functional theory

We investigate the mechanism of the stepwise formation of small neutral and cationic silver clusters in the gas phase and in solution using density functional theory (DFT) to study the evolving structures and free energies from Ag to Ag_{13}. Time-dependent density-functional theory (TDDFT) is used to calculate the corresponding UV-Vis spectra that could be compared with experiments. Our results are consistent with the predominance of kinetically stable cationic clusters observed in pulse radiolysis experiments.

As featured in:

See Jayendran C. Rasaiah *et al.*, *Phys. Chem. Chem. Phys.*, 2021, **23**, 25507.

ROYAL SOCIETY OF CHEMISTRY

rsc.li/pccp

Registered charity number: 207890

PCCP

ROYAL SOCIETY OF CHEMISTRY

PAPER

Cite this: *Phys. Chem. Chem. Phys.*, 2021, **23**, 25507

Theoretical study of the stability, structure, and optical spectra of small silver clusters and their formation using density functional theory†

Mohsen Farshad, Duwage C. Perera and Jayendran C. Rasaiah *

Received 4th September 2021,
Accepted 6th October 2021

DOI: 10.1039/d1cp04070g

rsc.li/pccp

An understanding of the mechanism of formation of small clusters would help to identify efficient routes to their synthesis. Here, we apply density functional theory (DFT) to study the free energies and structure of ultra-small silver clusters, and time-dependent density functional theory (TDDFT) to calculate their UV-Vis spectra and provide a better understanding of the intermediate steps in cluster formation in the gas phase and solution. Our calculations of the optical properties of neutral and cationic clusters confirm the presence of charged and uncharged intermediates observed in pulse radiolysis experiments during the early stages of the growth of silver clusters. The free energies of formation of hydrated clusters extracted from DFT calculations reveal the greater thermodynamic stability of cationic clusters compared to the corresponding neutral clusters of the same composition. This is consistent with the predominance of kinetically stable cationic clusters observed in pulse radiolysis experiments. Our DFT and TDDFT calculations clarify the effects of ligand, hydration, and oxidation states on the structure, stability, and optical properties of silver clusters that elucidate the mechanism of silver cluster formation in solution and the gas phase.

Nanoclusters (NCs) and sub-nanometer clusters (S-NCs) have drawn intensive research interest on account of their unique properties and potential applications in many fields such as catalysis,[1–8] medicine,[3,6–9] sensing,[3,6–10] optics,[1,3,6–11] and imaging.[3,6–13] An understanding of the mechanism of cluster formation in solution is essential to identify better synthetic routes to S-NCs and NCs of specific structure and size. This requires insights into the detailed steps of cluster nucleation and growth.

In general, nucleation and growth occur through dimerization and addition of metal ions or atoms to each other to form small clusters, followed by coalescence of clusters. Ultra-small nanoparticles in solution are stabilized by ligands that bind strongly to metal ions/atoms even in a homogeneously mixed solution, and therefore ligands modulate the mechanism of nanocluster formation. Along these lines, the kinetics of metal cluster formation and their size distribution was discussed recently[14,15] in ref. 14 and 15 following the early work by Lazzari, Jensen, and their colleagues.[16] The kinetic rate coefficients that are defined for each mechanistic step and the differential equations governing the kinetics of cluster formation were solved to predict their size distributions for plausible values of the rate coefficients. Our DFT calculations are the first steps towards determining these rate coefficients from first principles.[14,15]

Researchers have studied the earliest stages of metal cluster formation with pulse radiolysis techniques by detecting the UV-Vis bands of clusters during the earliest stage of their formation.[17] High energy pulses of radiation passed through an aqueous solution produce hydrated electrons ($H^{\bullet}$) that act as strong electron donors to reduce metal ions.[17–24] For example, hydrated electrons in an aqueous silver solution reduce Ag^{+} ions to Ag atoms (eqn (1)).

$$Ag^{+} + e \rightarrow Ag \quad (1)$$

Silver atoms are also routinely formed and studied in laboratories by adding a reducing agent to a solution containing silver ions.[18,19] Radiolysis studies show that silver atoms dimerize either with another silver ion (Ag^{+}) or neutral atoms (Ag).[18,19] Depending on the dosage of the pulses or the strength of the reducing agent, dimerization can occur through two pathways. At a very high reduction rate most Ag^{+} ions are quickly converted to neutral Ag atoms before further aggregation occurs. Consequently, Ag atoms bind to other uncharged Ag atoms to form Ag_2 dimers (eqn (2)):

Department of Chemistry, University of Maine, Orono, Maine 04469, USA.
E-mail: rasaiah@maine.edu

† Electronic supplementary information (ESI) available: The following files are available free of charge. Optimized structure of clusters in explicit water model, optical spectra of small clusters using a different number of virtual excitation states (PDF). See DOI: 10.1039/d1cp04070g

$$Ag + Ag \rightarrow Ag_2 \quad (2)$$

Conversely, for a weak reducing agent the probability of encounters between Ag atoms and Ag^+ ions is higher than between Ag atoms. In this case, the formation of charged Ag_2^+ dimers are statistically more likely (eqn (3)):

$$Ag + Ag^+ \rightarrow Ag_2^+ \quad (3)$$

Similarly, eqn (4) and (5) and eqn (6) and (7) show two pathways for the formation of trimers and tetramers in the presence of strong and weak reducing agents, respectively.

$$Ag_2 + Ag \rightarrow Ag_3 \quad (4)$$

$$Ag_2^+ + Ag^+ \rightarrow Ag_3^{2+} \quad (5)$$

$$Ag_2 + Ag_2 \rightarrow Ag_4 \quad (6)$$

$$Ag_2^+ + Ag_2^+ \rightarrow Ag_4^{2+} \quad (7)$$

The formation of clusters with different oxidation states (*e.g.*, Ag_3^+ and Ag_4^+) is also possible by intercrossing of growth pathways. Clusters can grow larger through addition of single silver ions or silver atoms to the seed clusters (eqn (8) and (9)), followed by their coalescence. The growth of NCs continues until they have reached a local minimum state in the free energy.

$$Ag_x^{a+} + Ag \rightarrow Ag_{x+1}^{a+} \quad (8)$$

$$Ag_x^{a+} + Ag^+ \rightarrow Ag_{x+1}^{(a+1)+} \quad (9)$$

$$Ag_x^{a+} + Ag_y^{b+} \rightarrow Ag_{x+y}^{(a+b)+} \quad (10)$$

Eqn (10) represents the coalescence of two silver NCs with x and y numbers of atoms and with charges a+ or b+ specified on the cluster. Zero charges correspond to a or b or both equal to zero.

The above mechanism is based on the assumption that ions even in a homogeneously mixed solution are not reduced simultaneously but are formed sequentially. Accordingly, successive peaks detected in the time-resolved UV-Vis spectra of radiolysis experiments were attributed to the sequential formation of Ag, Ag_2^+, Ag_3^{2+}, and Ag_4^{2+}.[17]

In this study we have performed systematic theoretical quantum mechanics (QM) calculations of the structure and energy of intermediates and products to better understand the mechanism of silver cluster formation by comparing them with the pulse radiolysis findings.[17] Furthermore, our QM studies clarify the effects of water ligands, hydration, and oxidation states on the structure, stability, and optical properties of the clusters. To this end, we used time-independent density functional theory (DFT) and time-dependent density functional theory (TDDFT) in which the Kohn–Sham (KS) equations are extended to time-dependent phenomena.

There have been several other DFT and TDDFT studies on metal clusters.[25–36] However, to our knowledge, there have been no extensive comparisons of QM calculations with pulse radiolysis experiments from a mechanistic perspective of ultrasmall cluster formation. In performing these calculations, we first optimized the structural geometries and determined the free energy of formation of selected clusters using DFT. Following this, we calculated the optical absorption of the optimized geometries using the linear response TDDFT.

1 Methods

The evaluation of exchange functionals and basis sets used in our calculations were improved by comparing existing TDDFT calculations with the optical bands of clusters observed in rare gas-phase spectroscopy experiments.[37–42] Harb *et al.* optimized different geometries of clusters at the DFT/BP86/LANL2DZ level of theory and performed TDDFT calculations with the same exchange functional and basis set to calculate the optical bands of the clusters.[32] They showed that the TDDFT/BP86/LANL2DZ level of theory has better predictive power for rare gas-phase experiments than other theories described in the literature.[32] For instance, their calculations on the Ag_4 cluster with D_{2h} planar symmetry and the Ag_5 cluster with C_{2v} planar symmetry, reproduced the two main peaks observed in rare gas-phase experiments. In our study, we applied the same level of theory using the Gaussian 16 package,[43] and the structures were optimized using DFT with the BP86 exchange functional[44,45] and LANL2DZ[46] effective core potential. Relativistic all-electron calculations are expensive, and the core potential that we employed is effective in reducing the calculation costs. From a chemical perspective, valence electrons are directly associated with the chemical behavior of an atom. The effective core potential is a reasonable approximation for describing a heavy atom. It incorporates the relativistic effects of heavy atoms implicitly with the use of a parametrized frozen core potential with respect to relativistic all-electron Hamiltonian results. Then we used the linear response TDDFT to compute the excited-state energies. As in our DFT calculations, we used the BP86 functional with LANL2DZ basis set for our TDDFT calculations. In our TDDFT calculations, we used single excitations with different numbers of excited electronic states of n = 25, 50, 75, and 100 for neutral and cationic clusters in each system that we studied. With the increase in the number of virtual excitation states, the probability of electronic excitations to higher energy levels increase, and therefore the optical band of clusters blue shifts toward lower wavelengths of energies. The relatively large number of virtual excited states allows us to capture most of the excitation energies.

Propagating real-time TDDFT is computationally difficult because integration over the time-dependent Schrodinger equation is computationally intensive and requires massive calculations for a many-body system. Therefore, linear-response TDDFT with a weak perturbative external potential was used to solve the Schrodinger equation. A one-to-one mapping of the linear response between the perturbed potential and density is the core of linear response TDDFT.

DFT and TDDFT calculations are performed at 0 K. Corrections to total energy for evaluating the enthalpy and Gibbs free energy to 298.15 K were achieved by using standard statistical

thermodynamics.[47] The translational, electronic, rotational, and vibrational contributions to partition functions are well known for non-interacting particles of an ideal system.[47] In our TDDFT calculations, the energy excitations of electrons were calculated from the lowest vibrational state of ground electronic state to the lowest vibrational states of excited electronic state (0–0 transition). At room temperature excitations can occur to higher vibrational states, however, at 298.15 K the kinetic energy is insufficient to promote electrons to jump to higher electronic levels.[48] To provide a rough statistical estimate of excitation energies of electrons excited from different vibrational states we broadened the excitation energies. A Gaussian function with a standard deviation of 0.4 eV was used to simulate the UV-Vis bands from calculated excitation energies. The standard deviation is the half-width of the Gaussian-shape band at ε_{max}/e, and it is proportional to the width of the spectrum.

DFT and TDDFT calculations on silver species were carried out in the gas phase, in the implicit aqueous solution phase, and in the presence of explicit water ligands from a single water molecule per atom in the cluster to an overall number of 25 water molecules. We did not perform the calculations with larger numbers of water molecules as it would have been computationally prohibitive for us. For implicit aqueous solution, we used an implicit solvent which is already implemented in Gaussian 16 package. In this case, we employed a self-consistent reaction-field model that builds a cavity in which the solute (silver species in our case) is placed in a continuum dielectric field.[49] A polarized continuum model (PCM) is widely used to outline the cavity in a dielectric field with a boundary condition that is manifested as charges on the surface of the cavity.[49] The cavity consists of spheres using Universal Force Field (UFF) radii with a scaling factor of 1.1 for the atomic radii of solute atoms. These spheres are centered at the solute atoms with an optimal volume slightly larger than solute, but it is problematic that the electron density of solute can expand beyond the boundary. However, in our calculations, an integral equation formalism of the PCM (IEFPCM) was employed to improve the boundary conditions and cope with the challenge that is introduced at the interface of solute electron density and cavity boundary.[49] We set the optimization criteria of the maximum force, root-mean-square (RMS) force, maximum displacement, and RMS displacement to 1.5×10^{-5}, 1×10^{-5}, 6×10^{-5}, and 4×10^{-5} Hartree respectively. The total energy conversion is set to a value within 10^{-9} Hartree.

2 Results and discussion

In our theoretical study, we first created clusters ranging in size from a single silver Ag to an Ag_{13} cluster with a full layer of twelve silver atoms around a single atom defined at the center of the cluster. These clusters are 0.7 nm or smaller in diameter, and consequently are subnanometer in size.[50,51] We optimized the structures and calculated the optical behavior of the clusters with the use of DFT and TDDFT methods respectively.

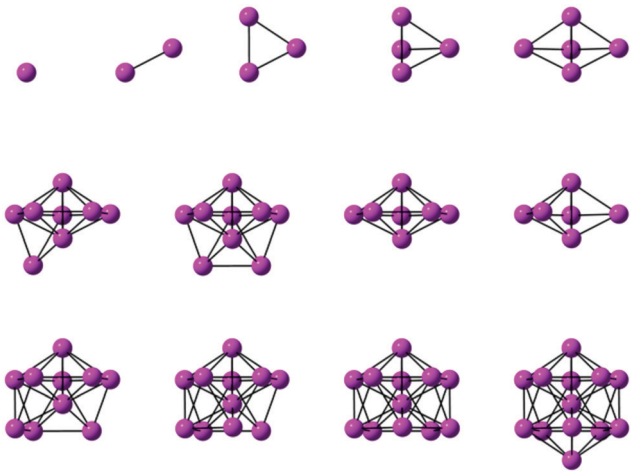

Fig. 1 Illustration of icosahedral Ag_{13} cluster formation from a single Ag atom.

We also investigated the effects of water molecules and an implicit water (IW) environment on the geometry and stability of the clusters.[52–54] Moreover, we studied their effects on electronic excitations with a different numbers of possible virtual excitation states and compared them with pulse radiolysis experiments.[52–54]

To construct the initial structures, we added a silver atom/ion to the preceeding structure consecutively at a position with the highest number of nearest neighbors at the same distances from the added atom. Our approach of building the first full-shell icosahedron cluster follows the Werfelmeier growth sequence of metal clusters explained extensively in Waless book on ''Energy Landscapes''.[55,56] Fig. 1 illustrates how this approach inherently leads to the formation of the Ag_{13} icosahedron.

We assumed that the addition of each ion/atom to a cluster during growth provides the lowest free energy pathway when the added ion/atom interacts with the highest number of constituents in the cluster at nearly equal distances. In this regard, for Ag_5 to Ag_{12} clusters, we selected initial structures that were consistent with the formation of icosahedral Ag_{13}. However, the optimized geometry of structures for some clusters changed considerably during this addition sequence (Fig. S1–S3, ESI†). In other cases, the symmetries of optimized clusters were similar to those obtained from the approach we took to form icosahedral Ag_{13}. For these cases, the lowest energies were obtained when the atoms/ions were bound to the maximum number of atoms/ions at approximately equal distances from each other. We searched for the most stable structures by optimizing the energy starting from different initial configurations.

Our calculations show that the Ag atom has a lower energy and consequently, greater stability than the Ag^+ ion. Mechanistically, after conversion of Ag^+ ions to Ag atoms through adsorption or transfer of electrons, the Ag atoms bind to another Ag^+ ion or Ag atom to form charged Ag_2^+ or neutral Ag_2 dimers respectively, which are obviously linear with

approximately similar stability under the same conditions. Our calculations reveal that Ag_2^+ has a greater bond length than Ag_2. In the gas phase, the bond lengths of Ag_2^+ and Ag_2 were 2.75 and 2.58 Å whereas the experimental values are 3.1 and 2.53 Å for bond lengths of the dimers detected by fluorescence spectroscopy in rare gas matrices[57] and far-infrared spectroscopy of zeolite pores[58] respectively. In an implicit aqueous solvent phase, we calculated bond lengths of 2.70 and 2.59 Å for Ag_2^+ and Ag_2, respectively. The Ag–Ag and Ag–O bond lengths for $Ag_2(H_2O)_2^+$ were calculated to be 2.71 and 2.25 Å, whereas for $Ag_2(H_2O)_2$ they were 2.58 and 2.36 Å. Addition of a third Ag^+ or Ag to Ag_2^+ or Ag_2 dimers sequentially formed equilateral or isosceles triangle structures of Ag_4^{2+} or Ag_3 trimers, respectively. Addition of Ag^+ or Ag to Ag_2 or Ag_2^+ formed an equilateral triangle Ag_3^+. Our results show that the cluster structures were affected by the oxidation states of the clusters and by whether water ligands are bound to them. In the gas phase, Ag_3^{2+} and Ag_3^+ formed equilateral triangle structures with each atom/ion bound to two atoms/ions at equal distances of 3.06 and 2.71 Å, respectively. Through the use of electron paramagnetic resonance, a triangular structure has been deduced for Ag_3^{2+} in zeolite cages.[59] The Ag–Ag bond length in Ag_3^{2+} has been measured to be 2.8–3.0 and 3.1 Å in zeolite cages using X-ray diffraction[59] and far-infrared[58] spectroscopy. Furthermore, a combination of DFT calculations and infrared multiple photodissociation spectroscopy in the gas phase have suggested an equilateral triangle structure for Ag_3^+ trapped in zeolite cages.[60] The change from an equilateral triangle for Ag_3^{2+} and Ag_3^+ to an isosceles triangle for Ag_3 is likely caused by the John–Teller effect in the electron density of states for the Ag_3 trimer owing to degeneracy of the ground state energy. In our calculations, the Ag–Ag and Ag–O bond lengths for $Ag_3(H_2O)_3^{2+}$ were 2.89 and 2.20 Å, and for $Ag_3(H_2O)_3^+$ they were 2.69 and 2.26 Å respectively. Both $Ag_3(H_2O)_3^{2+}$ and $Ag_3(H_2O)_3^+$ formed equilateral triangle structures.

Addition of another Ag atom to an uncharged Ag_3 or a charged Ag_3^{2+} ion trimer forms Ag_4 or Ag_4^{2+} tetramers, respectively. Furthermore, agglomeration of Ag_2^+ or Ag_2 dimers also produce Ag_4^{2+} or Ag_4 tetramers, respectively. On the conversion of charged Ag_4^{2+} to neutral Ag_4, the structure changed from tetrahedral to planar. To find stable structures for the charged and neutral tetramers we used planar and tetrahedral structures as the initial structures for Ag_4^{2+} and Ag_4. The Ag_4^{2+} and Ag_4 clusters reached equilibrium stability meeting the force and displacement criteria for energy minimization when the silver atoms reoriented to gain their tetrahedral and planer structures, respectively. In the gas phase, Ag_4^+ was optimized to both planar and distorted tetrahedral structures when the initial structures were planar or tetrahedral. Our calculations show that the distorted rhombus structure[61] of the naked Ag_4^+ in the gas and aqueous phases and $Ag_4(H_2O)_4^+$ was more stable than that of the tetrahedral conformer. For Ag_4^+ cluster, depending on the initial coordinates, the final coordinates were different whereas Ag_4^{2+} always formed a tetrahedron with an Ag–Ag bond length of 2.85 Å. Similarly, Ag_4 always formed a planner structure regardless of the initial structure. Our results show that, $Ag_4(H_2O)_4^{2+}$ is approximately tetrahedral with Ag–Ag and Ag–O distances of 2.80 and 2.22 Å respectively, compared with experimental values from luminescent-extended X-ray measurements of 2.82 and 2.36 Å.[62] In general, the Ag–O and Ag–Ag distances for clusters trapped in zeolite cages were approximately 2.8 and 2.2 Å, respectively, as extracted from X-ray diffraction measurements.[63] These values were closer to those from our calculations for cationic clusters. With 25 explicit water molecules, Ag_4 changed its orientation from planar to distorted geometry while Ag_4^+, Ag_4^{2+}, and Ag_4^{3+} optimized to tetrahedral structures (Fig. S1, ESI†). We should mention that initial planar Ag_4^{2+} optimized to tetrahedral structure and Ag_4^{3+} planar never optimized in our calculations.

To understand the thermodynamic stability of the optimized silver clusters, we calculated the free energy of formation of the smallest clusters using eqn (11):

$$\Delta G_{\left[\mathrm{Ag}_x(\mathrm{H_2O})_y\right]^{a+}} = G_{\mathrm{Ag}_x^{a+}} - (x-a)G_{\mathrm{Ag}_x} - aG_{\mathrm{Ag}_x^+} - yG_{\mathrm{H_2O}} \quad (11)$$

where x and a are the numbers of silver atoms and ions, respectively, that form the Ag_x^{a+} cluster, and y is the number of water molecules.

However, for implicit aqueous phase calculations using a polarized continuum model, the eqn (11) does not hold anymore as it does not evaluate the entropy of the species correctly. Empirically it has been discovered that species lose approximately half of their entropy upon solvation in water.[64,65] To account for this, we subtracted the enthalpy of each species from their free energy in the gas phase ($G_g - H_g$) and divided the result by two to calculate half of the entropy contribution ($-0.5TS_g$) to the free energy at 298.15 K. Then we added the enthalpy in aqueous phase to half of the entropy in gas phase (H_{aq}–$0.5TS_g$) to extract a new free energy for each species in the implicit aqueous phase.[66,67] Once this is done, we can plug in free energy values into eqn (11) to calculate the free energy of formation for each cluster.

Thermodynamic stability provides information on the growth pathway of silver clusters from an energetic perspective and their respective stable structures. Fig. 2 shows the free energy of formation of the most stable conformer of each species. Note that, the free energies of formation for some species are very close to each other. To clarify the relative stability of clusters with similar values, the vertical labels for species of each size are designated with respect to their formation free energies relative to each other (Fig. 2).

A silver cluster has a limit to the number of electrons and protons in its hydration shell. The structures were optimized in different ways to get the most stable forms. Fig. 2 shows that ionization or removal of an electron from some clusters decreases their free energy, whereas in others it does not. Hydration changes the order of the free energy of formation for clusters of the same size and different oxidation states as they change from the gas phase to phases where they are hydrated. The clusters with higher oxidation states such as Ag_3^{2+} and Ag_4^{3+} gain stability when they are bound to water reflecting greater electrostatic free energy of hydration, whereas

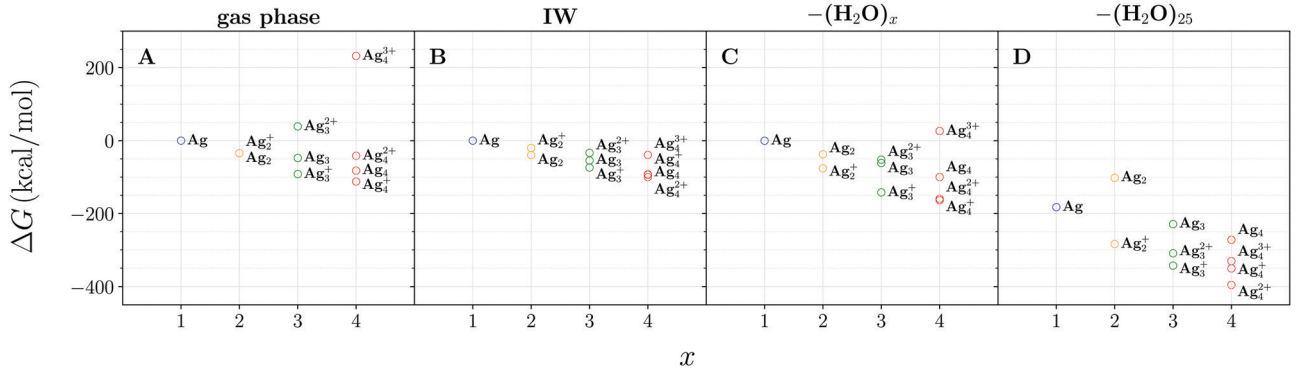

Fig. 2 Free energy of formation of silver species extracted from eqn (11) and DFT calculations of the respective silver species as described in the text for (A) gas phase, (B) aqueous implicit water phase (IW), (C) Ag_x^a clusters containing x silver atoms/ions with each hydrated by a single water molcule, and (D) explicit water model with 25 water molecules.

the stabilities of neutral Ag_3 and Ag_4 do not increase substantially except when there are many water molecules around them. This also implies that naked Ag_3^{2+} and Ag_4^{3+} cationic clusters acting as electrophiles are lacking electrons, and therefore are significantly unstable relative to the corresponding clusters with lower oxidation states. This effect is also evident in the Ag–O bond lengths of 2.2–2.6 Å in cationic clusters that shrink to 2.3–2.36 Å in neutral clusters.

The thermodynamics of small clusters determined in our calculations, especially in the presence of water ligands, support the hypothesis that kinetically stable charged clusters are formed during the early stages of growth. In the absence of a very strong reducing agent, there are less Ag atoms, and consequently, more Ag^+ cations aggregating to form charged clusters. Fig. 2 suggests similar paths of growth during the early stages of silver cluster formation in the gas and in implicit water phases and when the silver ion clusters are bound to water ligands. Our calculations show that hydrated silver species are more stable than their corresponding naked species in the gas phase. Fig. 2 also shows that water ligands, which act as electron donors to silver ions/atoms, stabilize the charged clusters.

Fig. 2D shows the free energy of formation for each Ag species hydrated by 25 water molecules. Our results for silver atoms/ions with many explicit water molecules strengthen the observation with the implicit water model. Each species has comparably lower free energy than in the gas phase or implicit solvent phase or with Ag clusters bonded to a few H_2O ligands. Based on our geometry optimization calculations, we considered the results only for distorted and the tetrahedral of neutral Ag_4 and its ions respectively.

We avoid discussion of clusters larger than tetramer because determining the most stable structures of large Ag clusters is difficult owing to the number of possible initial structures and limitations of our resources for DFT calculations. Therefore, we performed the DFT/TDDFT on only one possible structure for each of the clusters Ag_5 to Ag_{12} but two possible structures of icosahedral and cuboctahedral Ag_{13} because they have been well characterized and extensively referred to as stable structures for Ag_{13}.[56] The ligand effects on the structure of the clusters were revealed further in our DFT studies of Ag_{13} clusters.

Bare Ag_{13} form a roughly cuboctahedral structure, whereas hydrated Ag_{13} is present as a distorted cuboctahedron depending on the number of water molecules. Moreover, our implementation of DFT to determine the structure in an implicit aqueous solution predicts the formation of a distorted Ag_{13} icosahedron. The density of electrons governs the effects of oxidation state and ligands on the electronic structure of the clusters.

Table 1 Summarized calculated maxima of optical absorbance and free energy of formation for small charged and neutral silver clusters in the gas phase, implicit aqueous solution, and explicit aqueous solution with 25 water molecules (aqueous). For comparison, in the last column we insert the experimental values (Ex.) obtained from pulse radiolysis experiments![23,24,68]

	Gas phase	Implicit aqueous solution		Aqueous		Ex.	
System	(λ (nm))	ΔG (kcal mol)	λ (nm)	ΔG (kcal mol)	λ (nm)	ΔG (kcal mol)	λ (nm)
Ag	160, 300 (major)	0	180, 340 (major)	0	260	0	350–360
Ag_2	200, 280 (major), 400	−34.413	200, 280 (major), 400	−39.505	330	−37.584	
Ag_2^+	230 (major), 360	−34.181	280 (major), 430	−19.988	330	−75.900	−300 to 310
Ag_3	250, 350 (major), 390	−47.718	360	−54.465	310	−52.259	
Ag_3^+	200 (major), 320	−91.971	200 (major), 320	−73.870	260	−142.127	
Ag_3^{2+}	230, 330 (major)	39.232	250, 370 (major)	−33.533	260	−61.448	−265, 310
Ag_4	240, 300 (major), 450	−82.249	240, 310, 460 (major)	−93.643	300	−99.911	
Ag_4^+	280 (major), 400	−112.297	280 (major), 400	−92.429	320 (major), 450	−163.296	
Ag_4^{2+}	230, 270 (major)	−41.515	310	−100.196	320 (major), 530	−159.463	−270

Pulse radiolysis UV-Vis spectroscopy has enabled researchers to study the mechanism of metal cluster formation during their early stages of growth.[17] Time-resolved UV-Vis spectra are measured in radiolysis experiments during the successive formation of clusters with different emerging structures. However, because of instrumental limitations, it remains challenging to precisely characterize the optical absorption of specific clusters. To further elucidate the mechanism of silver cluster formation, we conducted TDDFT calculations on small silver clusters and compared our results with the spectra from pulse radiolysis experiments. Table 1 summarizes our calculated values with the experimental values. This table also includes a summary of our calculated free energy of the formation of corresponding clusters.

Our TDDFT calculations show that Ag^+ ions, unlike Ag atoms, do not have an absorption band above 200 nm (Fig. 3A) in either the gas phase or aqueous solution, but show a small peak around 240 nm and a dominant peak around 440 nm when there are explicit water molecules in the system. The absorption bands of Ag^+ and Ag are shifted to longer wavelengths in the implicit continuum water model and beyond in the presence of explicit water ligands representing hydration.

The experimental data from radiolysis studies do not have an absorption band for Ag^+ over 200 nm in agreement with our calculations except when there are water molecules around silver ion.[23,24] Fig. 3B shows the main absorption feature at 340 nm for Ag atoms in the aqueous phase (orange line), which corresponds to the first band that appears with a maximum in the range of 350–360 nm in radiolysis experiments soon after irradiation.[23,24] Fig. 3B shows that the main absorption band of Ag atom is at 300 nm in the gas phase (blue line). With the explicit water molecule model, the results (green line) deviate from radiolysis experiments, unlike the implicit water phase.

Fig. 4A shows the spectrum for a charged Ag_2^+ dimer. Two distinguishable maxima over 200 nm change their positions on moving from the gas phase (blue line) to the implicit aqueous solution (orange line). In radiolysis experiments, the absorption band at a maximum of 300–310 nm is attributed to Ag_2^+.[23,24] The absorption band of the charged Ag_2^+ dimer hydrated with 25 H_2O molecules, had a maximum at 340 nm (Fig. 4A green line). Fig. 3B shows three peaks for the neutral dimer Ag_2 with a major peak in the range from 270 to 290 in gas and implicit water environments, which is close to the 300–310 nm experimental peak. This is also relatively close to the peak of Ag_2 in explicit water around 330 nm.

Aggregation of Ag_2^+ or Ag_2 with Ag^+ or Ag form trimers Ag_3^{2+}, Ag_3^+ and Ag_3 respectively. Fig. 5A shows that in the gas phase the major band had a maximum at 330 nm in the gas phase and two absorption bands at 250 and 370 nm in the implicit solution phase. In Fig. 5A the Ag_3^{2+} ionic cluster in the solution shows one band with a maximum at 260 nm (green line). Fig. 5B, Ag_3^+ had two peaks at 200 and 320 nm (blue and orange lines)

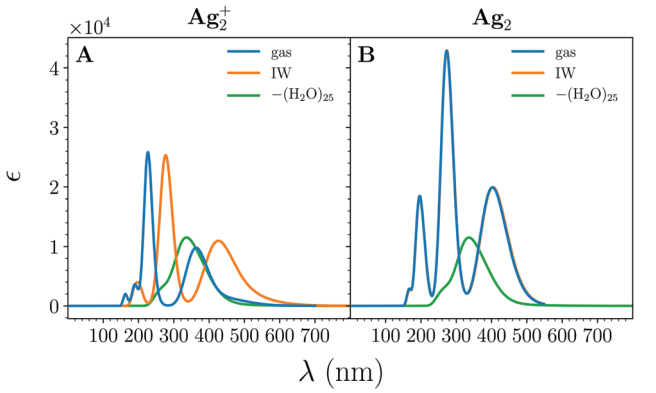

Fig. 4 Calculated optical bands of Ag_2^+ and Ag_2 from TDDFT at the BP86/LANL2DZ level of theory with n = 50 excited electronic states. (A) Absorption spectra of Ag_2^+ in gas phase (blue line) and an implicit aqueous phase (orange line), and spectra of Ag_2^+ with 25 water molecules (green line). (B) Absorption spectra of Ag_2 in gas phase (blue line) and an implicit aqueous phase (orange line), and spectra of Ag_2 with 25 water molecules (green line).

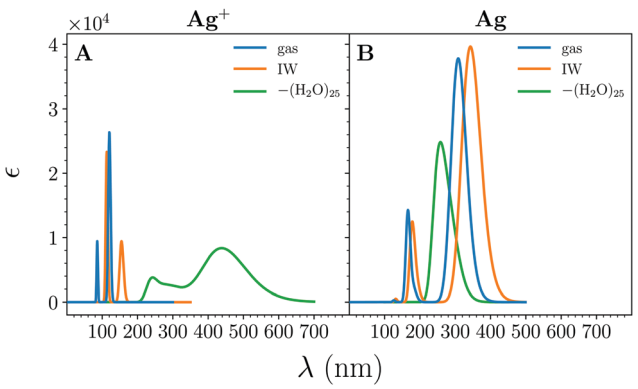

Fig. 3 Calculated optical bands of Ag^+ and Ag using TDDFT at the BP86/LANL2DZ level of theory with n = 50 excited electronic states. (A) Absorption spectra of Ag^+ in the gas phase (blue line) and an implicit aqueous phase (orange line), and spectra of Ag with 25 water molecules (green line). (B) Absorption spectra of Ag in the gas phase (blue line) and an implicit aqueous phase (orange line), and spectra of Ag with 25 water molecules (green line).

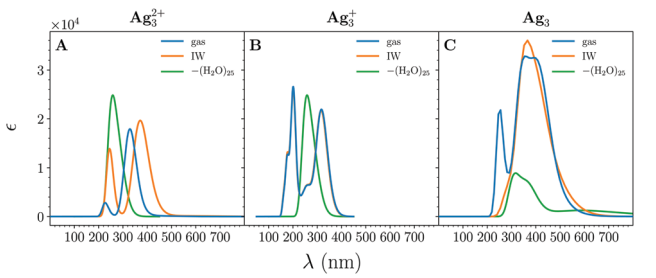

Fig. 5 Optical band of Ag_3^{2+}, Ag_3^+, and Ag_3 calculated by TDDFT at the BP86/LANL2DZ level of theory with n = 50 excited electronic states. (A) Absorption spectra of Ag_3^{2+} in the gas phase (blue line) and an implicit aqueous phase (orange line), and spectra of Ag_3^{2+} with 25 water molecules (green line). (B) Absorption spectra of Ag_3^+ in gas phase (blue line) and an implicit aqueous phase (orange line), and spectra of Ag_3^+ with 25 water molecules (green line). (C) Absorption spectra of Ag_3 in gas phase (blue line) and an implicit aqueous phase (orange line), and spectra of Ag_3 with 25 water molecules (green line).

in gas and aqueous phases. The Ag_3^+ spectrum in explicit water shown in Fig. 5B (green line) has one major peak at 260 nm. Two maxima in the radiolysis experiments were at 310 and 265 nm.[68] In this regard, the TDDFT calculations of charged clusters produced peaks at 260 nm for Ag_3^{2+} and Ag_3^+ in explicit water, and 320 nm for Ag_3^{2+} and Ag_3^+ in gas phase are close to the experimental absorption maxima at 265 and 310 nm.[68] Neutral Ag_3 cluster generates a peak around 310 nm in explicit water and a peak around 250 nm in gas phase, which are also close to experimental absorption peaks.

The Ag_4^{2+} tetramer can form through addition of Ag^+ ions to the Ag_3^+ trimer and agglomeration of two Ag_2^+ dimers eqn (6) and (7). In our calculations, formations of Ag_4^+ and Ag_4 were also considered. Fig. 6A shows that the absorption bands of Ag_4^{2+} has peaks between 220–300 nm. In the gas phase, the main maximum was at 270 nm (blue line), and in the implicit aqueous solution, it was at 310 nm (orange line). The absorption bands of the Ag_4^{2+} with 25 explicit water molecules appeared at 320 nm and 500–550 nm (green line). Fig. 6B shows similar peak patterns at 280 nm and 400 nm in both the gas phase and the implicit water phase while there is one major peak at 320 nm in the explicit water shell. In radiolysis experiments the maximum at 270 nm, which was generated as a successive peak after irradiation of the silver ion solution, is attributed to Ag_4^{2+},[23,24] which is comparable with spectra in gas and implicit solvent for both neutral and charged silver species. Fig. 6C shows that the neutral tetramer Ag_4 spectra also contain peaks in the region between 235–305 nm in the gas and aqueous phases, which is close to the experimentally measured absorption that has a maximum at 270 nm. There is only one major peak at 300 nm for the neutral Ag_4 species with 25 water molecules (green line).

The absorption peaks calculated in this study for both sets of charged Ag_2^+, Ag_3^+, Ag_3^{2+}, Ag_4^+, and Ag_4^{2+} and neutral Ag_2, Ag_3, and Ag_4 clusters conform approximately to the observed maxima in the radiolysis experiments. We mention that the optical peaks calculated from different virtual excitation states of n = 25, 50, 75, and 100 were similar, as presented in Fig. S4–S7 (ESI†).

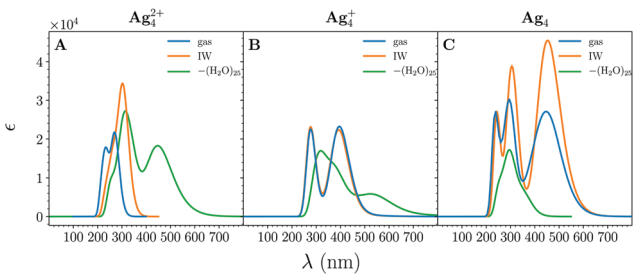

Fig. 6 Optical band of Ag_4^{2+}, Ag_4^+, and Ag_4 calculated by TDDFT at the BP86/LANL2DZ level of theory with n = 50 excited electronic states. (A) Absorption spectra of Ag_4^{2+} in the gas phase (blue line) and an implicit aqueous phase (orange line), and spectra of Ag_4^{2+} with 25 water molecules (green line). (B) Absorption spectra of Ag_4^+ in gas phase (blue line) and an implicit aqueous phase (orange line), and spectra of Ag_4^+ with 25 water molecules (green line). (C) Absorption spectra of Ag_4 in gas phase (blue line) and an implicit aqueous phase (orange line), and spectra of Ag_4 with 25 water molecules (green line).

As previously mentioned, for clusters larger than Ag_4 we only studied neutral clusters owing to the complexity of the problem for clusters with many atoms. Nonetheless, in pulse radiolysis experiments, it is difficult to assign optical absorptions for clusters larger than tetramers, and the mechanism of cluster formation is inferred from data for the formation of smaller clusters.[17]

For the Ag_x clusters with x = 5–12, the maxima of optical bands shift to higher wavelengths as more excited electronic states become available in the gas and aqueous phases. Furthermore, our results indicate that the extinction coefficient of the absorption bands increased from Ag_5 to Ag_8 in the gas and aqueous phases; however, the absorption intensity did not change notably from Ag_9 to Ag_{12} for either the gas phase or aqueous solution (Fig. 7A–P).

The calculated absorption bands show that the absorption maxima for clusters Ag_5 to Ag_{12} are located between 300–400 nm. In radiolysis experiments, the bands that appeared in later stages of growth with maxima between 300–400 nm are attributed to oligomers larger than Ag_4^{2+}. Also, it is evident that the absorption band of clusters blue shifts to lower wavelength with an increase of available excited states from 25 to 100 nm. As the number of virtual possible excited states increases, the probability of excitations to higher-level orbitals such as 5d or excitations from 4d to s + p orbitals in silver clusters increases, and there can be a possibility of the shift of spectra to higher energies.

Fig. 8 shows the optical bands of a full shell cluster Ag_{13} in the gas phase and aqueous solution, and when the number of water molecules as ligands increases from two to eight. The absorption bands for Ag_{13} under different conditions were around and above 500 nm, *i.e.*, longer wavelengths than those of the Ag_{12} bands that were around and below 400 nm in the aqueous phase and gas phase respectively.

In this work, we used TDDFT to calculate the UV-Vis spectra of S-NCs complementary to the results of pulse radiolysis experiments.[17] The excitation energies facilitated our assignment of the absorption bands from the smallest clusters detected in radiolysis experiments. UV-Vis spectral characterization is important for understanding the mechanism of S-NCs and NC formation. Growth of nanoparticles occurs through monomer and ion addition to the cluster and coalescence of clusters.[14,15]

The structures of clusters are determined by the silver atoms or ions with their associated charges, ligands, and the solvent environment. We created silver clusters of different sizes and performed DFT calculations on them to predict the electronic structure and stability of the clusters in the gas phase, in the presence of water ligands, and solution. Then we used TDDFT to calculate the optical bands of the clusters in the gas phase, in the presence of water ligands, and/or in the solution phase. The outcome of this work will be informative in confirming and characterizing the properties of silver clusters reported in experimental studies and also provide insight into the

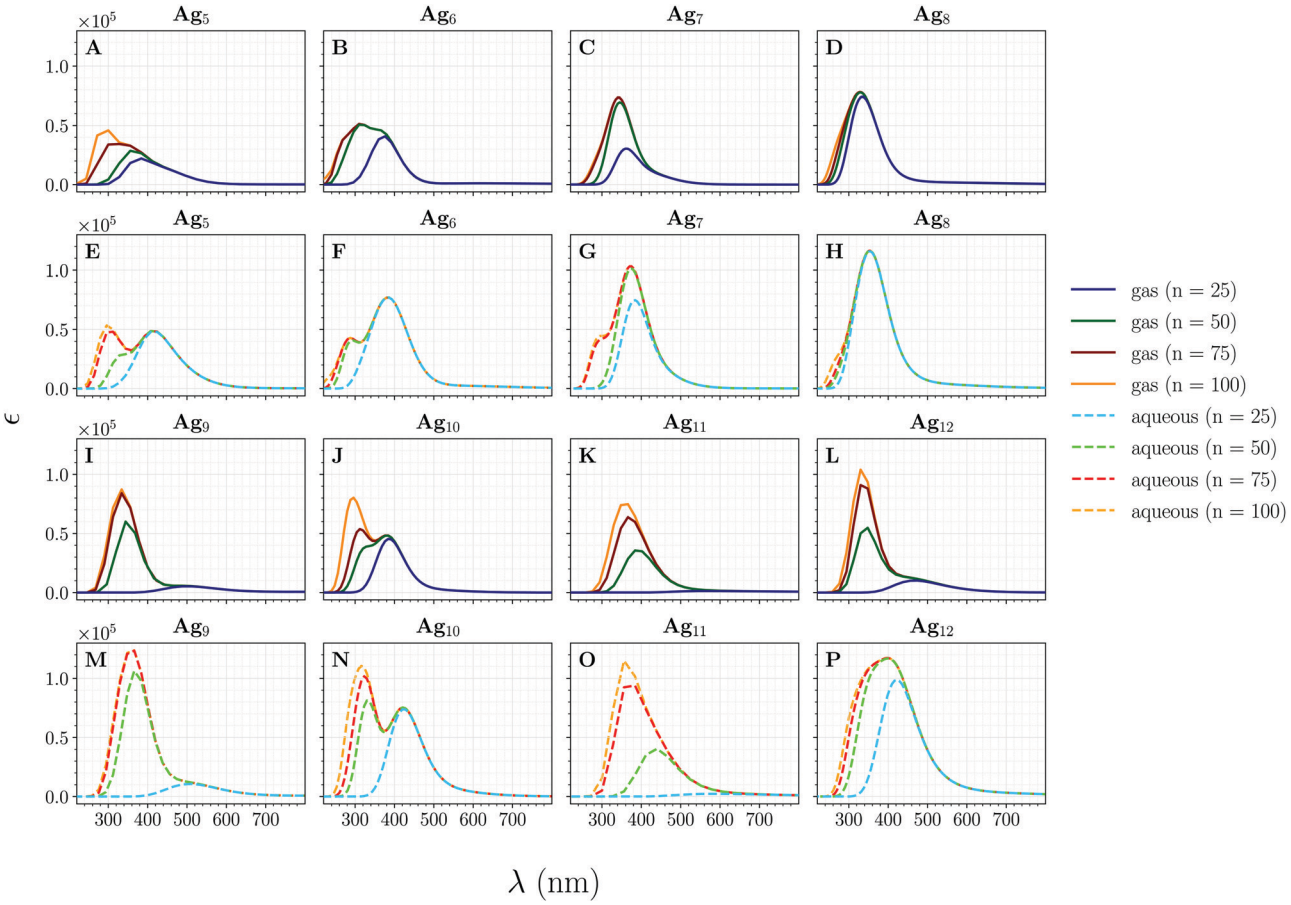

Fig. 7 Absorption spectra of Ag_x (x = 5–12) with n = 25, 50, 75, and 100 excited electronic states in gas phase (A–D, I–L) and in implicit aqueous solution (E–H, M–P). The TDDFT simulated spectra partially matched the radiolysis results; however, finding a more accurate method to reproduce the experimental results will require further investigation.

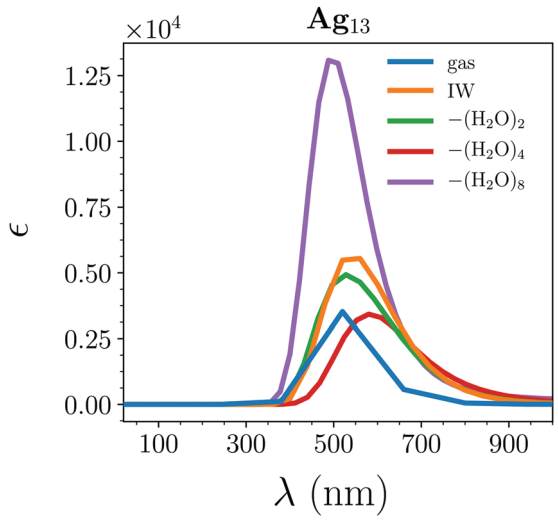

Fig. 8 Calculated optical band of Ag_{13} using TDDFT at the BP86/LANL2DZ level of theory with n = 50 excited electronic states. Absorption spectra of Ag_{13} in the gas phase (blue line) and implicit aqueous phase IW (orange line), and spectra of $Ag_{13}(H_2O)_x$ for x = 2, 4, and 8 shown with green, red, and purple lines, respectively.

mechanism of their formation. Our study does not confirm either ion addition or atom addition pathways of growth. However, it does indicate the strong possibility of the involvement of both pathways based upon their stability of the intermediates and comparison of their optical absorptions to pulse radiolysis experiments.

The plethora of spurious excited states caused mainly by nearly degenerate low lying states of nd to (n + 1)s transitions or charge transfer transitions[69] are not apparent in the spectra of Ag clusters calculated with BP86/LANL2DZ level of theory (described in Methods). BP86 is a generalized gradient approximation (GAA) exchange functional that is lacking long-range electron–electron interactions. The long-range correction (LC) to the exchange functionals, LC-BP86, incorporates long-range interaction to GGA exchange functional by using Hartree–Fock functionals at long range.[70–72] The number of spurious excited states with LC-functionals in UV-Vis region (above 200 nm) decrease significantly.[71,72] These spurious states have usually low absorption intensities and do not interfere noticeably with the main absorption spectra of small silver clusters.[71] It has been shown that the BP86 long-range asymptotic potential is

effective in reproducing experimental spectra with a relatively small LANL2DZ basis set in the regions of our concern.[32] However, there is a considerable difference in the spectra of large clusters (Ag_{18} and Ag_{20}) obtained from BP86 and LC-BP86.[71] These differences are attributed to plasmon-like bands of mainly s to s + p transitions captured with incorporation of long-range interactions in LC-functionals.[72–74]

This study can be extended to a systematic investigation of clusters ranging from the smallest ones to clusters larger than 2 nm, which may lead to a fundamental understanding of plasmons and their activity. Plasmons are collective oscillations of electrons across large clusters rather than single excitations in small clusters.[75–78] Studying the optical bands of small and large clusters provides information on the behavior of electrons during interactions with light, which may explain the plasmon inactivity of small clusters. Furthermore, the DFT method is effective for understanding the effects of ligands on the electronic excitations of clusters and how they are involved in the excitation of electrons in small and large clusters. Lastly, obtaining spectra of small clusters at 298 K extracted from the molecular mechanics QM (QMMM) method with an appropriate level of theory potentially can provide a more realistic comparison with experimental spectra at room temperature. That is beyond the scope of this work, which We leave for a future study.

Our study of the mechanism of subnanometer and nanometer cluster formation provides information about the geometry, stability, and optical properties of small naked and solvated clusters in different oxidation states and the larger icosahedron Ag_{13}. We show in detail the effect of explicit water ligands on these properties. We find that the choice of the number of virtual excited states affects the spectra of clusters significantly.

3 Conclusions

In this study we used DFT and thermodynamic calculations to probe the structure and stability of ultra-small silver NCs and their ions, in the gas and solution phases and the mechanism of cluster formation by comparing our TDDFT calculations of the UV-Vis spectra with results from pulse radiolysis experiments. Our calculations of clusters with different oxidation states facilitated the assignments of peaks in the UV-Vis spectra of transient species in radiolysis experiments during the formation of clusters in their early stages of growth. The similarity of spectra obtained from TDDFT calculations and those from pulse radiolysis experiments conforms to either ion or monomer addition growth pathways in the formation of cationic and neutral clusters. Moreover, our free energy calculations suggest that the formation of cationic clusters is energetically favored over neutral clusters. The presence of conventional reducing agents causes an abundance of Ag^+ relative to Ag, which kinetically favors the formation of cationic clusters through the ion addition pathway. Energy optimization of DFT calculations reveal the effects of oxidation state, ligands, and hydration on the structure and optical properties of the silver clusters. However, a complete deterministic elucidation of the growth pathways would require further theoretical and experimental investigations on small clusters. This study is a step in that direction.

Conflicts of interest

There are no conflicts to declare.

Acknowledgements

We thank Dr François G. Amar and Dr Brian G. Frederick for their comments and discussions on this study and two referees for their incisive comments. We acknowledge the editorial assistance of Dr Jackson. The authors are grateful for supercomputer time provided by the Advanced Computing Group at the University of Maine and in particular Stephen Cousins for his continuous support.

References

1 R. Jin, *Nanoscale*, 2015, **7**, 1549–1565.
2 E. Fernandez and M. Boronat, *J. Phys.: Condens. Matter*, 2019, **31**, 013002.
3 Y. Lu and W. Chen, *Chem. Soc. Rev.*, 2012, **41**, 3594.
4 L. Liu and A. Corma, *Chem. Rev.*, 2018, **118**, 4981–5079.
5 J. Fang, B. Zhang, Q. Yao, Y. Yang, J. Xie and N. Yan, *Coord. Chem. Rev.*, 2016, **322**, 1–29.
6 I. Chakraborty and T. Pradeep, *Chem. Rev.*, 2017, **117**, 8208–8271.
7 R. Jin, C. Zeng, M. Zhou and Y. Chen, *Chem. Rev.*, 2016, **116**, 10346–10413.
8 Y. Tao, M. Li, J. Ren and X. Qu, *Chem. Soc. Rev.*, 2015, **44**, 8636–8663.
9 Y. Su, T. Xue, Y. Liu, J. Qi, R. Jin and Z. Lin, *Nano Res.*, 2019, **12**, 1251–1265.
10 L. Zhang and E. Wang, *Nano Today*, 2014, **9**, 132–157.
11 B. Du, X. Jiang, A. Das, Q. Zhou, M. Yu, R. Jin and J. Zheng, *Nat. Nanotechnol.*, 2017, **12**, 1096–1102.
12 Q. Zhang, M. Yang, Y. Zhu and C. Mao, *Curr. Med. Chem.*, 2018, **25**, 1379–1396.
13 L. Shang, S. Dong and G. U. Nienhaus, *Nano Today*, 2011, **6**, 401–418.
14 M. Farshad, D. Suvlu and J. C. Rasaiah, *J. Phys. Chem. C*, 2019, **123**, 29954–29963.
15 D. Suvlu, M. Farshad and J. C. Rasaiah, *J. Phys. Chem. C*, 2020, **124**, 17340–17346.
16 S. Lazzari, P. M. Theiler, Y. Shen, C. W. Coley, A. Stemmer and K. F. Jensen, *Langmuir*, 2018, **34**, 3307–3315.
17 J. Belloni, J.-L. Marignier and M. Mostafavi, *Radiat. Phys. Chem.*, 2020, **169**, 107952.
18 A. Henglein, *Chem. Rev.*, 1989, **89**, 1861–1873.
19 J. Belloni, *Radiat. Res.*, 1998, **150**, S9.

20 *Clusters of Atoms and Molecules*, ed. H. Haberland, V. I. Goldanskii, F. P. Schäfer, J. P. Toennies and H. K. V. Lotsch, Springer Berlin Heidelberg, Berlin, Heidelberg, 1994, vol. 52.

21 A. Henglein, B. G. Ershov and M. Malow, *J. Phys. Chem.*, 1995, **99**, 14129–14136.

22 J. Belloni, M. Mostafavi, H. Remita, J.-L. Marignier and A. M.-O. Delcourt, *New J. Chem.*, 1998, **22**, 1239–1255.

23 B. G. Ershov, E. Janata, A. Henglein and A. Fojtik, *J. Phys. Chem.*, 1993, **97**, 4589–4594.

24 M. Mostafavi, G. R. Dey, L. François and J. Belloni, *J. Phys. Chem. A*, 2002, **106**, 10184–10194.

25 S. Klacar, A. Hellman, I. Panas and H. Grönbeck, *J. Phys. Chem. C*, 2010, **114**, 12610–12617.

26 M. Amft, B. Sanyal, O. Eriksson and N. V. Skorodumova, *J. Phys.: Condens. Matter*, 2011, **23**, 205301.

27 D. H. Wells, W. N. Delgass and K. T. Thomson, *J. Chem. Phys.*, 2002, **117**, 10597–10603.

28 R. C. Baetzold, *J. Phys. Chem. C*, 2017, **121**, 11811–11823.

29 N. Durante, A. Fortunelli, M. Broyer and M. Stener, *J. Phys. Chem. C*, 2011, **115**, 6277–6282.

30 M. Kuisma, A. Sakko, T. P. Rossi, A. H. Larsen, J. Enkovaara, L. Lehtovaara and T. T. Rantala, *Phys. Rev. B: Condens. Matter Mater. Phys.*, 2015, **91**, 115431.

31 M. Harb, F. Rabilloud and D. Simon, *Chem. Phys. Lett.*, 2009, **476**, 186–190.

32 M. Harb, F. Rabilloud, D. Simon, A. Rydlo, S. Lecoultre, F. Conus, V. Rodrigues and C. Félix, *J. Chem. Phys.*, 2008, **129**, 194108.

33 R. L. Gieseking, M. A. Ratner and G. C. Schatz, *J. Phys. Chem. A*, 2016, **120**, 4542–4549.

34 G.-T. Bae and C. M. Aikens, *J. Phys. Chem. C*, 2012, **116**, 10356–10367.

35 S. Kahlal, C. W. Liu and J.-Y. Saillard, *Inorg. Chem.*, 2017, **56**, 1209–1215.

36 M. Chen, J. E. Dyer, K. Li and D. A. Dixon, *J. Phys. Chem. A*, 2013, **117**, 8298–8313.

37 S. Fedrigo, W. Harbich and J. Buttet, *Phys. Rev. B: Condens. Matter Mater. Phys.*, 1993, **47**, 10706–10715.

38 W. Harbich, S. Fedrigo and J. Buttet, *Z. Phys. D: At., Mol. Clusters*, 1993, **26**, 138–140.

39 B. Collings, K. Athanassenas, D. Rayner and P. Hackett, *Chem. Phys. Lett.*, 1994, **227**, 490–495.

40 H. Haekkinen, B. Yoon, U. Landman, X. Li, H.-J. Zhai and L.-S. Wang, *J. Phys. Chem. A*, 2003, **32**(107), 6168–6175.

41 C. Yu, R. Schira, H. Brune, B. von Issendorff, F. Rabilloud and W. Harbich, *Nanoscale*, 2018, **10**, 20821–20827.

42 R. Schira and F. Rabilloud, *J. Phys. Chem. C*, 2018, **122**, 27656–27661.

43 M. J. Frisch, G. W. Trucks, H. B. Schlegel, G. E. Scuseria, M. A. Robb, J. R. Cheeseman, G. Scalmani, V. Barone, G. A. Petersson, H. Nakatsuji, X. Li, M. Caricato, A. V. Marenich, J. Bloino, B. G. Janesko, R. Gomperts, B. Mennucci, H. P. Hratchian, J. V. Ortiz, A. F. Izmaylov, J. L. Sonnenberg, D. Williams-Young, F. Ding, F. Lipparini, F. Egidi, J. Goings, B. Peng, A. Petrone, T. Henderson, D. Ranasinghe, V. G. Zakrzewski, J. Gao, N. Rega, G. Zheng, W. Liang, M. Hada, M. Ehara, K. Toyota, R. Fukuda, J. Hasegawa, M. Ishida, T. Nakajima, Y. Honda, O. Kitao, H. Nakai, T. Vreven, K. Throssell, J. A. Montgomery, Jr., J. E. Peralta, F. Ogliaro, M. J. Bearpark, J. J. Heyd, E. N. Brothers, K. N. Kudin, V. N. Staroverov, T. A. Keith, R. Kobayashi, J. Normand, K. Raghavachari, A. P. Rendell, J. C. Burant, S. S. Iyengar, J. Tomasi, M. Cossi, J. M. Millam, M. Klene, C. Adamo, R. Cammi, J. W. Ochterski, R. L. Martin, K. Morokuma, O. Farkas, J. B. Foresman and D. J. Fox, *Gaussian 16, Revision C.01*, Gaussian Inc., Wallingford, CT, 2016.

44 A. D. Becke, *Phys. Rev. A: At., Mol., Opt. Phys.*, 1988, **38**, 3098–3100.

45 J. P. Perdew, *Phys. Rev. B: Condens. Matter Mater. Phys.*, 1986, **33**, 8822–8824.

46 P. J. Hay and W. R. Wadt, *J. Chem. Phys.*, 1985, **82**, 270–283.

47 J. W. Ochtershi, *Thermochemistry in Gaussian*, Gaussian Inc., Wallingford, CT, 2000.

48 M. Hodecker, M. Biczysko, A. Dreuw and V. Barone, *J. Chem. Theory Comput.*, 2016, **12**, 2820–2833.

49 J. Tomasi, B. Mennucci and R. Cammi, *Chem. Rev.*, 2005, **105**, 2999–3094.

50 S. Ahlert, W. Klein, O. Jepsen, O. Gunnarsson, O. K. Andersen and M. Jansen, *Angew. Chem., Int. Ed.*, 2003, **42**, 4322–4325.

51 C. Amano, H. Niina and Y. Mikami, *THEOCHEM*, 2009, **904**, 64–68.

52 V. Dubois, P. Archirel and A. Boutin, *J. Phys. Chem. B*, 2001, **105**, 9363–9369.

53 V. Dubois, M. Seijo and P. Archirel, *Chem. Phys. Lett.*, 2004, **389**, 150–154.

54 A. Boutin, R. Spezia, F.-X. Coudert and M. Mostafavi, *Chem. Phys. Lett.*, 2005, **409**, 219–223.

55 W. Wefelmeier, *Z. Phys.*, 1937, **107**, 332–346.

56 D. J. Wales, *Energy landscapes*, Cambridge University Press, Cambridge, UK; New York, 2003.

57 B. Simard, P. A. Hackett, A. M. James and P. R. Langridge-Smith, *Chem. Phys. Lett.*, 1991, **186**, 415–422.

58 M. D. Baker, G. A. Ozin and J. Godber, *J. Phys. Chem.*, 1985, **89**, 305–311.

59 J. Michalik and L. Kevan, *J. Am. Chem. Soc.*, 1986, **108**, 4247–4253.

60 J. van der Tol, D. Jia, Y. Li, V. Chernyy, J. M. Bakker, M. T. Nguyen, P. Lievens and E. Janssens, *Phys. Chem. Chem. Phys.*, 2017, **19**, 19360–19368.

61 A. Shayeghi, R. L. Johnston and R. Schäfer, *Phys. Chem. Chem. Phys.*, 2013, **15**, 19715.

62 D. Grandjean, E. Coutio-Gonzalez, N. T. Cuong, E. Fron, W. Baekelant, S. Aghakhani, P. Schlexer, F. D'Acapito, D. Banerjee, M. B. J. Roeffaers, M. T. Nguyen, J. Hofkens and P. Lievens, *Science*, 2018, **361**, 686–690.

63 T. Miyanaga, H. Hoshino and H. Endo, *J. Synchrot. Radiat.*, 2001, **8**, 557–559.

64 D. H. Wertz, *J. Am. Chem. Soc.*, 1980, **102**, 5316–5322.

65 M. H. Abraham, *J. Am. Chem. Soc.*, 1981, **103**, 6742–6744.

66 J. Kua, S. W. Hanley and D. O. De Haan, *J. Phys. Chem. A*, 2008, **112**, 66–72.
67 J. K.-C. Lau and D. V. Deubel, *J. Chem. Theory Comput.*, 2006, **2**, 103–106.
68 E. Janata, *Radiat. Phys. Chem.*, 2012, **81**, 1404–1406.
69 C. J. Cramer and D. G. Truhlar, *Phys. Chem. Chem. Phys.*, 2009, **11**, 10757.
70 T. Tsuneda and K. Hirao, *Wiley Interdiscip. Rev.: Comput. Mol. Sci.*, 2014, **4**, 375–390.
71 M. Harb, F. Rabilloud and D. Simon, *J. Phys. B: At., Mol. Opt. Phys.*, 2011, **44**, 035101.
72 F. Rabilloud, *J. Phys. Chem. A*, 2013, **117**, 4267–4278.
73 R. Schira and F. Rabilloud, *J. Phys. Chem. C*, 2019, **123**, 6205–6212.
74 D. W. Silverstein and L. Jensen, *J. Chem. Phys.*, 2010, **132**, 194302.
75 J. Yan, Z. Yuan and S. Gao, *Phys. Rev. Lett.*, 2007, **98**, 216602.
76 J. Yan and S. Gao, *Phys. Rev. B: Condens. Matter Mater. Phys.*, 2008, **78**, 235413.
77 C. M. Aikens, S. Li and G. C. Schatz, *J. Phys. Chem. C*, 2008, **112**, 11272–11279.
78 R. Zhang, L. Bursi, J. D. Cox, Y. Cui, C. M. Krauter, A. Alabastri, A. Manjavacas, A. Calzolari, S. Corni, E. Molinari, E. A. Carter, F. J. García de Abajo, H. Zhang and P. Nordlander, *ACS Nano*, 2017, **11**, 7321–7335.